Journal of Translational Medicine

RESEARCH

Open Access

Intratumoral microbiota-aided fusion radiomics model for predicting tumor response to neoadjuvant chemoimmunotherapy in triple-negative breast cancer

Yilin Chen[1,2†], Yuhong Huang[2†], Wei Li[3,4†], Teng Zhu[2], Minyi Cheng[2], Cangui Wu[2], Liulu Zhang[2], Hao Peng[2*] and Kun Wang[1,2*]

Abstract

Background Neoadjuvant chemoimmunotherapy (NACI) has emerged as the standard treatment for early-stage triple-negative breast cancer (TNBC). However, reliable biomarkers for identifying patients who are likely to benefit from NACI are lacking. This study aims to develop an intratumoral microbiota-aided radiomics model for predicting pathological complete response (pCR) in patients with TNBC.

Methods Intratumoral microbiota are characterized by 16S rDNA sequencing and quantified through experimental assays. Single-cell RNA sequencing is performed to analyze the tumor microenvironment of tumors with various responses to NACI. Radiomics features are extracted from tumor regions on longitudinal magnetic resonance images (MRIs) scanned before and after NACI in the training set. On the basis of treatment response (pCR or non-pCR) and intratumoral microbiota scoring, we select key radiomics features and construct a fusion model integrating multi-timepoint (pre-NACI and post-NACI) MRI to predict the efficacy of immunotherapy, followed by independent external validation.

Results A total of 124 patients are enrolled, with 88 in the training set and 36 in the validation set. Tumors from patients who achieves pCR present a significantly greater intratumoral microbiota load than tumors from patients who achieve non-pCR ($p < 0.05$). Additionally, tumors in non-pCR group exhibit greater infiltration of tumor-associated $SPP1^+$ macrophages, which is negatively correlated with the microbiota load. On the basis of intratumoral microbiota scoring, we select 17 radiomics features and use them to construct the fusion radiomics model. The fusion model achieves the highest AUC of 0.945 in the training set, outperforming pre-NACI (AUC = 0.875) and post-NACI (AUC = 0.917) models. In the validation set, this model maintains a superior AUC of 0.873, surpassing those of pre-NACI (AUC = 0.769) and post-NACI (AUC = 0.802) models. Clinically, the fusion model distinguishes patients who achieve pCR from those who do not with an accuracy of 77.8%. Decision curve analysis demonstrates the superior net clinical benefit of this model across varying risk thresholds.

†Yilin Chen, Yuhong Huang and Wei Li have equally contributed to this study.

*Correspondence:
Hao Peng
phao@gdph.org.cn
Kun Wang
gzwangkun@126.com
Full list of author information is available at the end of the article

Conclusions Our intratumoral microbiota-aided radiomics model could serve as a powerful and noninvasive tool for predicting the response of patients with early-stage TNBC to NACI.

Keywords Triple-negative breast cancer, Intratumoral microbiota, Radiomics, Neoadjuvant chemoimmunotherapy

Background

Triple-negative breast cancer (TNBC) is the most aggressive subtype of breast cancer, and it is associated with unsatisfactory survival outcomes due to the lack of effective targeted therapies [1–4]. Recent progress in TNBC research has suggested that neoadjuvant anti-PD1 therapy in addition to chemotherapy is associated with significantly improved pathological complete response (pCR) and long-term survival outcomes [5–7]. Therefore, neoadjuvant chemoimmunotherapy (NACI) has become the preferable strategy for treating early-stage TNBC. However, the addition of pembrolizumab resulted in only an approximately 5% absolute improvement in the 5-year overall survival rate (86.6% vs. 81.7%), indicating that most patients do not benefit from the addition of immunotherapy. This highlights the urgent need for reliable biomarkers to screen patients who are likely to benefit from this treatment approach and thus avoid overtreatment.

More than 10% of cancer cases are associated with infections [8], and the microbiome has been reported to be involved in tumorigenesis and disease progression [9–15]. Moreover, increasing data highlight that tumor microbiome is a potential modulator of immune responses and therapeutic efficacy across multiple cancer types [16, 17]. Intriguingly, specific bacterial populations within the tumor can modulate the immune landscape by producing metabolites that impact immune cell behavior, such as T cell activation and cytokine secretion, which may promote or suppress antitumor responses [17–20]. These studies suggest that tumor microbiota may serve as a specific and robust biomarker for the prediction of immunotherapy efficacy. However, monitoring the tumor microbiota requires invasive and time-consuming approaches, and samples are easily contaminated by laboratory environments; thus, the clinical application of this approach is limited. Therefore, development of a noninvasive, easy and accurate tool for monitoring tumor microbiota is crucial for the use of individualized NACI strategies to treat cancer.

Radiomics, which extracts high-throughput data-characterization algorithms for translation into high-dimensional and quantitative imaging features, has gained recognition as a non-invasive approach to assess tumor heterogeneity, immune phenotypes, and potentially microbiota-associated features [21, 22]. By quantifying imaging features such as shape, texture, and intensity, MRI radiomics has been used to characterize biological processes, including immune cell infiltration and PD-L1 expression [22–25], which are important for predicting immunotherapy outcomes. Hence, radiomics has been widely developed as a noninvasive and time-saving method for clinical decision-making [26–28]. However, whether radiomics could serve as a tool for monitoring tumor microbiota and tumor response to NACI in patients with TNBC remains unstudied.

Here, we explored and validated the association between intratumoral microbiota and tumor response to NACI in TNBC. Moreover, we performed single-cell transcriptome analysis to elucidate the immune microenvironment landscape of tumors with different responses to NACI, and analyzed the correlation between intratumoral microbiota and tumor microenvironment (TME). Finally, we developed an MRI radiomics model to monitor intratumoral microbiota and tumor response to NACI.

Methods

Study patients

Eligible patients with TNBC diseases treated between June 2020 and May 2024 at Guangdong Provincial People's Hospital (training set) and the First People's Hospital of Foshan (validation set) were enrolled for this study if they: (i) had newly diagnosed TNBC without distant metastasis; (ii) aged 18–70 years; (iii) did not receive prior anti-cancer treatments; (iv) received NACI and radical surgery; (v) did not combined with other malignancies; (vi) had complete dynamic contrast-enhanced MRI (DCE-MRI) data before and after NACI. The study was approved by the Research Ethics Committee of Guangdong Provincial People's Hospital and the First People's Hospital of Foshan. Written informed consent for the use of patient specimens and corresponding medical data was obtained from each participant.

Treatment strategy

NACI regimens included nab-paclitaxel (260 mg/m^2, d1) plus carboplatin (AUC 5, d1) and anti-PD1 (200 mg, d1) every 3 weeks for 4 cycles followed by epirubicin (75 mg/m^2, d1) plus cyclophosphamide (600 mg/m^2, d1) and anti-PD1 (200 mg, d1) every 3 weeks for 4 cycles, or nab-paclitaxel (260 mg/m^2, d1) plus carboplatin (AUC 5, d1) and anti-PD1 (200 mg, d1) every 3 weeks for 4–6 cycles. After the completion of NACI, patients received radical

surgery including modified mastectomy, breast-conserving surgery (BCS) with sentinel lymph node biopsy (SLNB) or axillary lymph node dissection (ALND) and nipple-sparing mastectomy (NSM) with SLNB or ALND.

16S rDNA sequencing (16S-seq)

Tissue DNA were extracted from frozen pre-treatment samples of 57 patients (22 with non-pCR and 35 with pCR) at Guangdong Provincial People's Hospital using the DNA extraction kit. The V3-V4 region of bacterial 16S rRNA was amplified for library construction and sequenced on the Illumina Nova6000 platform (Magigene Biotechnology Co, China). Detailed information on 16S-seq and data analysis was shown in Additional file.

Single-cell transcriptome sequencing (scRNA-seq)

Fresh pre-treatment tissues of 6 patients (3 with non-pCR and 3 with pCR) were washed by Hanks Balanced Salt Solution (HBSS) and then dissociated into single-cell suspensions which were forwarded to reverse transcription and library construction. Then, libraries were pooled and sequenced on Illumina novaseq 6000 with 150 bp paired end reads (Singleron, China). Detailed information on scRNA-seq and data analysis was shown in Additional file.

Real-time quantitative polymerase chain reaction (RT-qPCR)

Total RNAs were extracted from frozen pre-treatment tissues of 65 patients (25 with non-pCR and 40 with pCR) at Guangdong Provincial People's Hospital using TRIzol reagent (Life Technologies, USA). A total of 2 μg of RNA were reverse-transcribed to cDNA which was subjected to real-time quantification. Detailed information was shown in Additional file.

Fluorescence in situ hybridization (FISH)

Paraffin-embedded slides of pre-treatment tissues were dewaxed, rehydrated and then subjected to antigen retrieval. After pre-hybridization at 37 °C for 1 h, slides were incubated with the pan-bacterial 16S rRNA probe (EUB338-GCTGCCTCCCGTAGGAGT) at 40 °C overnight followed by DAPI staining at room temperature for 5–10 min. Images were obtained by a Nikon upright fluorescence microscope. For quantification of 16S rRNA expression, we randomly selected three fields of view for each section and calculated the intensity of each field of view. Then, we took the average of three fields of view as the expression level of this section. Detailed information was shown in Additional file.

Immunohistochemistry (IHC) staining

Paraffin-embedded slides of pre-treatment tissues were deparaffinized in xylene, rehydrated in ethanol gradient, then incubated with 3% H_2O_2 followed by antigen retrieval. Following that, slides were blocked by 5% TBST-BSA buffer for 1 h and then incubated with primary anti-LPS (Hycult Biotech, Netherlands) at 4 ℃ overnight. After incubation with secondary antibody, targeted proteins were stained by DAB reagent (DAKO, Denmark). For quantification of LPS expression, we randomly selected three fields of view for each section and calculated the intensity of each field of view. Then, we took the average of three fields of view as the expression level of this section. Detailed information was shown in Additional file.

Multiplex immunofluorescence staining

Paraffin-embedded slides of pre-treatment tissues from 10 patients (5 with non-pCR and 5 with pCR) were dewaxed, rehydrated and then subjected to antigen retrieval. After being blocked by TBST-BSA buffer, slides were incubated with primary antibody at 4 ℃ overnight followed by incubation with secondary antibody and then stained by TSA solution at room temperature for 10 min. Subsequently, slides underwent antigen retrieval, blocking, incubation with primary and secondary antibodies repeatedly until all targeted proteins were labelled. Finally, slides were stained by DAPI before images capture. Detailed information was shown in Additional file.

MRI acquisition

Each patient underwent pre-NACI and post-NACI breast MRI scans. To ensure comparability between the two time points, the same scanner and imaging protocol were used for each patient. The MRI scanning protocol included T1-weighted, T2-weighted, diffusion-weighted, and dynamic contrast-enhanced (DCE) imaging. MRI scans were performed using standardized parameters across all centers, ensuring consistency in field strength (1.5 T or 3 T), spatial resolution, and acquisition timing. MRI images underwent rigorous quality control to exclude artifacts such as motion or incomplete coverage. To address MRI scan inconsistencies, we applied the N4ITK MRI Bias Correction tool to mitigate intensity non-uniformities caused by magnetic field variations. MRI images were resampled to a uniform voxel size of 1 mm^3 using linear interpolation, eliminating anisotropy. Additionally, we normalized the grayscale intensity of MRI images to a 0–1000 range, followed by histogram matching to standardize intensity distributions across

all images. These preprocessing steps ensured consistent and reliable extraction of radiomics features.

Tumor region delineation

Tumor regions of interest (ROIs) were delineated manually on DCE images experienced radiologists using 3D Slicer (version 4.10.2). Both radiologists performed the segmentations independently under a double-blind protocol. For pre-NACI MRI, ROIs were delineated around the primary tumor. For post-NACI MRI, the tumor bed was identified based on residual enhancement, changes in anatomical structure, and associated features such as fibrosis or edema. To ensure reproducibility, inter- and intra-rater reliability was evaluated using Dice similarity coefficients, achieving a coefficient > 0.9.

Radiomics feature extraction

To avoid batch effects and ensure data quality, feature extraction followed the Image Biomarker Standardization Initiative guidelines. Radiomics features were extracted from the ROIs on both pre-NACI and post-NACI images. The PyRadiomics tool was used to extract a comprehensive feature set, including first-order statistics, shape-based and texture features. Additionally, wavelet-transformed features were calculated to capture multi-scale tumor characteristics.

Radiomics feature selection

Feature selection was conducted separately for pre-NACI and post-NACI feature sets to identify the most relevant predictors associated with pCR and intratumoral microbiome score. Initially, the Mann–Whitney U test was applied to identify features significantly associated with the pCR ($p < 0.05$). Features with high inter-correlation (Spearman correlation coefficient $|r| > 0.9$) were excluded to avoid multicollinearity. Only one feature from each correlated group was retained based on the stronger univariate association with the intratumoral microbiome score. Subsequently, elastic net regression was used to select the most important features based on the intratumoral microbiome score. The optimal hyperparameters (α and λ) for the elastic net model were determined using tenfold cross-validation, minimizing mean squared error and maximizing model performance.

Model development

The modeling process used data from Center 1 as the training set and data from Center 2 as the independent validation set. Three logistic regression models were constructed separately for the pre-NACI features, post-NACI features, and a combining feature set to predict the pCR. For each model, the regularization strength L2 penalty were optimized using tenfold cross-validation on the training set. Model performance was assessed using the receiver operating characteristic (ROC) curve and precision-recall (PR) curve for the training and validation sets. Comprehensive classification metrics was evaluated, including area under the receiver operating characteristic curve (AUC), sensitivity, specificity, and accuracy. The robustness of three models was evaluated using bootstrap resampling (1000 iterations) to estimate confidence intervals for AUCs. Calibration plots and decision curve analysis (DCA) were conducted to assess the clinical utility and reliability of the model.

Statistical analysis

All statistical analyses were performed using Python (version 3.8) and R (version 4.3) software. Continuous variables were summarized as mean ± standard deviation or median with interquartile range, depending on the Shapiro–Wilk test. Categorical variables were presented as counts and percentages. Differences between groups were compared using the Mann–Whitney U test for continuous variables and the Chi-square or Fisher's exact test for categorical variables. To compare model performance across the pre-NACI, post-NACI, and fusion models, the DeLong test was used to assess differences in AUC. Calibration was assessed using the Hosmer–Lemeshow test, with bootstrapping used to estimate confidence intervals of performance metrics. Statistical significance was defined as a two-sided $p < 0.05$.

Results

Patient characteristics

A total of 145 eligible female patients were screened, and 124 patients with early-stage TNBC treated with NACI and surgery between June 2020 and January 2024 were enrolled in this study; 88 patients from Guangdong Provincial Peoples's Hospital served as the training set, and 36 patients from the First People's Hospital of Foshan served as the validation set (Fig. 1). NACI resulted in a total pCR rate of 62.1% (77/124), and patients were grouped according to their tumor response to NACI (pCR vs. non-pCR). The patients' baseline characteristics were shown in Table 1. Among the 124 patients, 67.7% (84/124) were diagnosed with stage I-II disease, whereas only 8 (6.5%) patients presented with N_3 disease. Clinical tumor stages were well balanced between the pCR and non-pCR groups in both training and validation sets ($p > 0.05$ for all comparisons). Intriguingly, the pCR group had significantly greater percentages of patients with pathological grade III disease than the non-pCR group in both training (70.9% vs. 43.3%, $p = 0.013$) and validation sets (95.5% vs. 64.3%, $p = 0.014$). As expected, the percentage of patients who underwent sentinel lymph node biopsy (SLNB) in pCR group was significantly greater

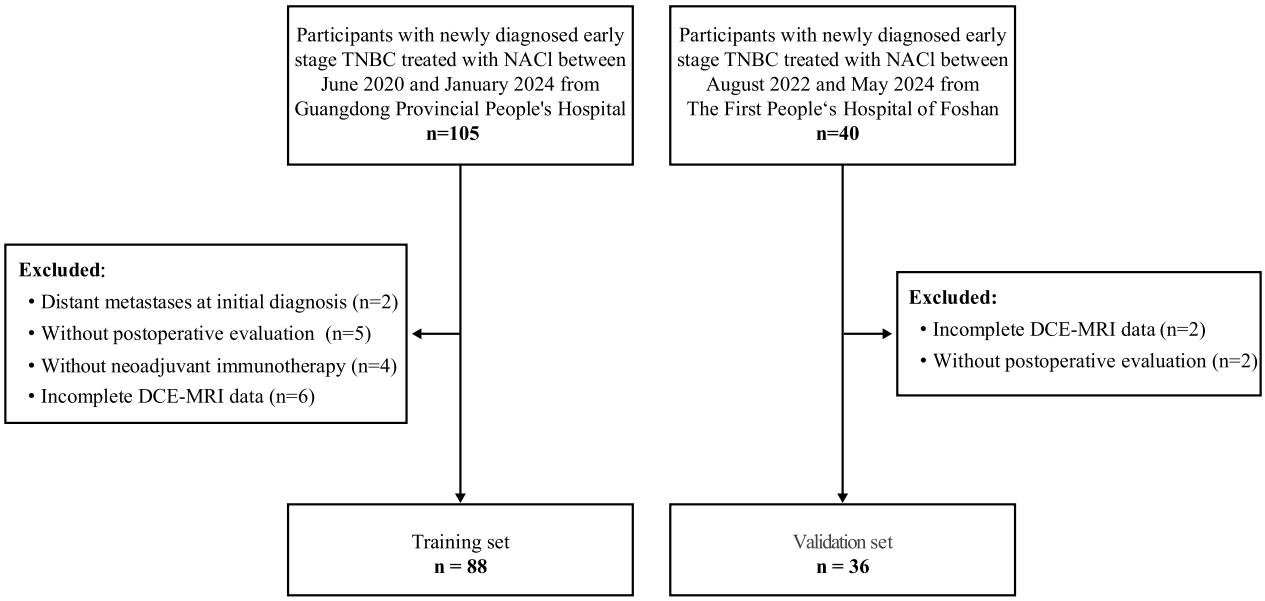

Fig. 1 Flowchart of study patient enrollment. TNBC: triple-negative breast cancer; NACI: neoadjuvant chemoimmunotherapy: DCE-MRI: dynamic contrast-enhanced magnetic resonance imaging

than that in non-pCR group in the training set (50.9% vs. 27.3%, p = 0.0442).

Intratumoral microbiota was positively correlated with tumor response to NACI

To confirm the presence of intratumoral microorganisms in TNBC tissues, we performed 16S rDNA sequencing (16S-seq) on pretreatment biopsy samples from 57 patients (35 in pCR group and 22 in non-pCR group) in the training set. After standard procedures of contamination filtration, a broad spectrum of bacterial communities at both phylum and class levels were identified in TNBC tissues (Fig. 2A). We subsequently determined the intratumoral microbiota load of tumors from pCR and non-pCR groups. Real-time quantitative polymerase chain reaction (RT-qPCR) analysis of 16S rDNA revealed that the intratumoral microbiota load was significantly greater in pCR group than in non-pCR group (p < 0.0001; Fig. 2B). Next, we developed a standard curve for the absolute quantification of intratumoral microbiota load by RT-qPCR, and the results confirmed that still tumors from pCR group had a significantly greater load than tumors from non-pCR group (p < 0.0001; Fig. 2C and D). Moreover, both fluorescence in situ hybridization analysis of 16S rDNA and immunohistochemical staining of bacterial LPS protein revealed that intratumoral microbiota load was significantly greater in pCR group than in non-pCR group (Fig. 2E–H). Nevertheless, we also evaluated the association between intratumoral microbiota load and tumor response assessed by radiological methods. Tumors with a radiology-defined complete response (CR) presented a significantly greater intratumoral bacterial load than those without CR (Fig. 2I, J). Taken together, these findings suggested a positive correlation between intratumoral microbiota load and the pathological tumor response in patients undergoing NACI, indicating that intratumoral microbiota may serve as a specific and robust biomarker for screening populations who are likely to benefit from NACI.

Intratumoral microbiota was positively associated with an activated TME

To gain insight into the TME of tumors with different responses to NACI, we performed single-cell transcriptome sequencing (scRNA-seq) on 6 samples (3 in pCR group and 3 in non-pCR group). A total of 61,266 single cells from 7 clusters were identified, which included 33,923 epithelial cells, 1111 endothelial cells (ECs), 1134 mural cells, 2274 B cells, 11,764 T cells, 5434 plasma cells and 5626 mononuclear phagocytes (MPs; Fig. 3A–C). Intriguingly, compared with those of tumors from non-pCR group, the TME of tumors from pCR group presented decreased levels of MPs and elevated levels of plasma cells (Fig. 3C). With respect to macrophages, a total of 5 subclusters were identified (Fig. 3D, E). As anticipated, the tumors from pCR group had significantly greater $FOLR2^{+}$ macrophage infiltration (46.0% vs. 21.8%), whereas tumors from non-pCR group presented more $SPP1^{+}$ macrophages (22.22% vs. 5.76%; Fig. 3F). In addition, 6 subclusters

Table 1 Baseline characteristics of patients enrolled in this study

Characteristic	Training cohort			Validation cohort		
	pCR (No, %)	Non-pCR (No, %)	p[a]	pCR (No, %)	Non-pCR (No, %)	p[a]
Median age (range)	47 (28–70)	53 (30–66)	0.045	50 (26–72)	50 (27–62)	0.973
T stage[b]			0.234			0.108
T1	6 (10.9)	3 (9.1)		7 (31.8)	0 (0)	
T2	36 (65.5)	21 (63.6)		9 (40.9)	10 (71.4)	
T3	11 (20)	4 (12.1)		5 (22.7)	3 (21.4)	
T4	2 (3.6)	5 (15.2)		1 (4.6)	1 (7.2) 90	
N stage[b]			0.082			0.261
N0	26 (47.3)	11 (33.3)		1 (4.5)	3 (21.4)	
N1	19 (34.5)	10 (30.3)		20 (90.9)	10 (71.4)	
N2	9 (16.4)	7 (21.2)		0 (0)	0 (0)	
N3	1 (1.8)	5 (15.2)		1 (4.6)	1 (7.2)	
Overall stage[b]			0.486			0.693
I	1 (1.8)	1 (3.0)		0 (0)	0 (0)	
II	37 (67.3)	18 (54.6)		16 (72.7)	11 (78.6)	
III	17 (30.9)	14 (42.4)		6 (17.3)	3 (21.4)	
Chemo-IM regimen			0.811			0.152
NACI regimen			0.296			1.000
Nab-pac/Carbo + anti-PD1	21 (38.2)	9 (27.3)		0 (0)	0 (0)	
EC-TCb + anti-PD1	34 (31.8)	24 (72.7)		22 (100)	14 (100)	
Pathological Grade[c]			0.013			0.014
I–II	16 (29.1)	17 (56.7)		1 (4.5)	5 (35.7)	
III	39 (70.9)	13 (43.3)		21 (95.5)	9 (64.3)	
Median Ki67 (range)	75 (20–95)	62.5 (10–95)	0.024	45 (20–95)	60 (20–90)	0.711
Surgery			0.144			0.755
BCS + SLNB	11 (20)	1 (3.0)		0 (0)	0 (0)	
BCS + ALND	8 (14.5)	7 (21.2)		9 (40.9)	5 (35.7)	
Mastectomy + SLNB	14 (25.5)	8 (24.2)		0 (0)	0 (0)	
Mastectomy + ALND	12 (21.8)	10 (30.3)		13 (59.1)	9 (64.3)	
NSM + SLNB	3 (5.5)	0 (0)		0 (0)	0 (0)	
NSM + ALND	7 (12.7)	7 (21.2)		0 (0)	0 (0)	

pCR: pathological complete response; non-pCR: non-pathological complete response; Nab-pac: albumin-bound paclitaxel; Carbo: carboplatin; anti-PD-1: Sintilimab or Camrelizumab or Pembrolizumab; EC: epirubicin plus cyclophosphamide; TCb: paclitaxel plus carboplatin; BCS: breast-conserving surgery; SLNB: sentinel lymph node biopsy; ALND: axillary lymph node dissection; NSM: nipple-sparing mastectomy

[a] p values were calculated by the Chi-square test for categorical variables and student's t test for continuous variables

[b] According to the 8th edition of the International Union against Cancer/American Joint Committee on Cancer (UICC/AJCC) staging manual

[c] Three patients in Guangdong Provincial People's Hospital did not have such data

of plasma cells were identified (Fig. 3G, H). The tumors from pCR group had more IGHM$^+$ plasma cells (53.29% vs. 12.14%), whereas tumor from non-pCR group presented with more HSP90AA1$^+$ plasma cells (70.14% vs. 16.72%; Fig. 3I). As SPP1$^+$ macrophages have been widely proven to be a tumor-promoting immunosuppressive cells [29–34], we therefore validated the expression of SPP1$^+$ macrophage in tumors from pCR and non-pCR groups by multiplex immunofluorescence (mIF) staining. Consistent with the data of scRNA-seq, the mIF data confirmed the increased infiltration of SPP1$^+$ macrophages into tumors from non-pCR group ($p = 0.0018$; Fig. 3J, K). Moreover, the number of SPP1$^+$ macrophages was negatively correlated with the intratumoral microbiota load (Fig. 3L, M). Taken together, these results revealed the distinct landscape of TME between pCR and non-pCR groups and suggested that intratumoral microbiota may affect tumor response to NACI by altering the TME.

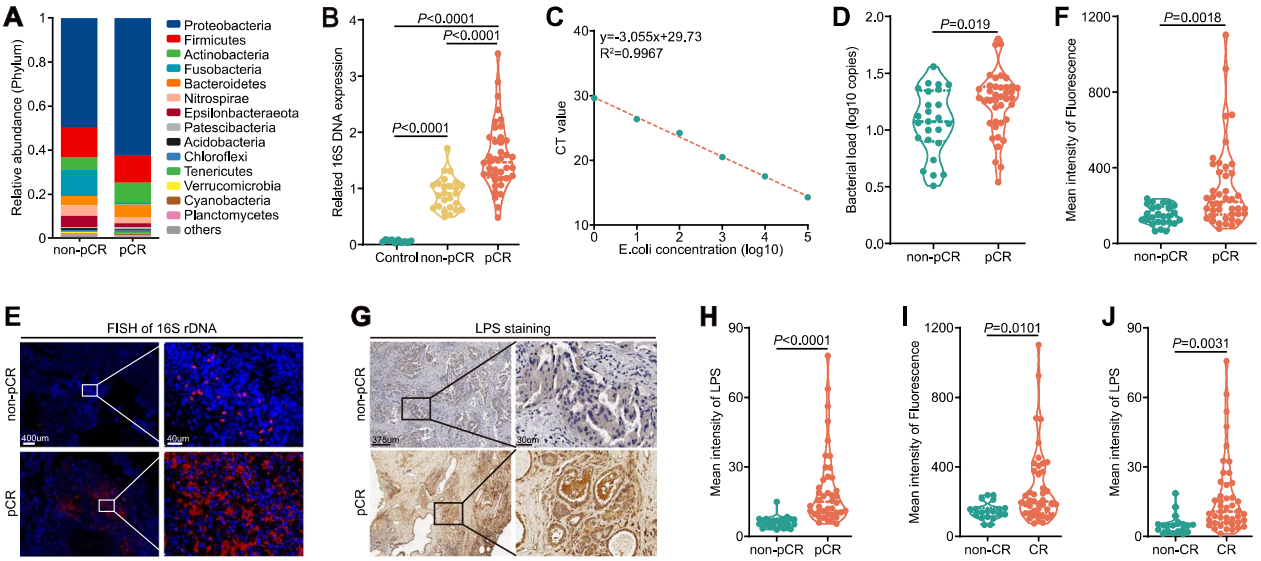

Fig. 2 Intratumoral microbiota load was positively correlated with tumor response to NACI. **A** Relative abundance of the top 15 taxa at phylum level in TNBC tissues identified by 16S-seq. **B** RT-qPCR analysis of 16S rDNA in negative control (n = 10), pCR (n = 40) and non-pCR (n = 25) tumors. **C** Standard curve used for absolute quantification of intratumoral microbiota load via RT-qPCR assay. **D** RT-qPCR analysis of absolute intratumoral microbiota load of pCR (n = 40) and non-pCR tumors (n = 25). **E**, **F** FISH staining of 16S rDNA in pCR (n = 42) and non-pCR tumors (n = 26). Scale bars, left panels, 400 μm; right panels, 40 μm. **G**, **H** IHC staining of LPS in pCR (n = 42) and non-pCR tumors (n = 25). Scale bars, left panels, 375 μm; right panels, 30 μm. **I** Statistical analysis of 16S rDNA as revealed by FISH staining between radiology-defined CR (n = 43) and non-CR tumors (n = 19). **J** Statistical analysis of LPS in radiology-defined CR (n = 44) and non-CR tumors (n = 19)

Feature extraction and selection

Having elucidated the correlation between intratumoral microbiota and tumor response to NACI, we then developed a microbiota-aided radiomic model to predict tumor responses. A total of 1223 radiomics features were extracted for each time point, including first-order, shape-based, texture and wavelet features. The Mann–Whitney U test revealed that 278 pre-NACI and 395 post-NACI features were significantly associated with pCR. Spearman correlation analysis further eliminated highly correlated features, leaving 212 and 306 features. Elastic net regression further retained the optimal feature sets associated with intratumoral microbiome score, including 9 pre-NACI features and 8 post-NACI features. The correlation matrix revealed that each feature was an independent predictor of NCAI (Fig. 4A and B).

Models performance and comparison

In the training set, the fusion model achieved the highest AUC of 0.945, outperforming the pre-NACI (AUC = 0.875) and post-NACI (AUC = 0.917) models, indicating improved classification capability when both pre-NACI and post-NACI data were integrated (Fig. 4C). Precision-recall curves demonstrated a consistent improvement in sensitivity and precision of the fusion model (Fig. 4D). Decision curve analysis revealed that the fusion model provided superior net clinical benefit across a range of risk thresholds compared with single-time-point models (Fig. 4E). In the validation set, the fusion model maintained superior performance (AUC = 0.873), exceeding those of the pre-NACI model (AUC = 0.769) and the post-NACI model (AUC = 0.802). This model demonstrated better precision and recall balance in predicting pCR (Fig. 4F and G). Decision curve analysis further confirmed the robustness of the fusion model (Fig. 4H), which consistently had greater net benefits than did the single-time-point model. These findings demonstrated the added value of incorporating pre-NACI and post-NACI data, indicating that the fusion model could make better predictions.

Clinical validation of models

The confusion matrices for the fusion, pre-NACI, and post-NACI models were analyzed to evaluate their clinical value (Fig. 5). In the training set, the fusion model achieved the highest sensitivity (96.3%, 52/54), specificity (88.2%, 30/34), and accuracy (93.2%, 82/88), effectively distinguishing patients with pCR from those without with minimal misclassification. In comparison, the pre-NACI model had a sensitivity of 90.7% (49/54), and a specificity of 79.4% (27/34), and the post-NACI model had a sensitivity of 92.6% (50/54) but a lower specificity of 73.5% (25/34). In the validation set, the fusion model maintained strong performance, with a

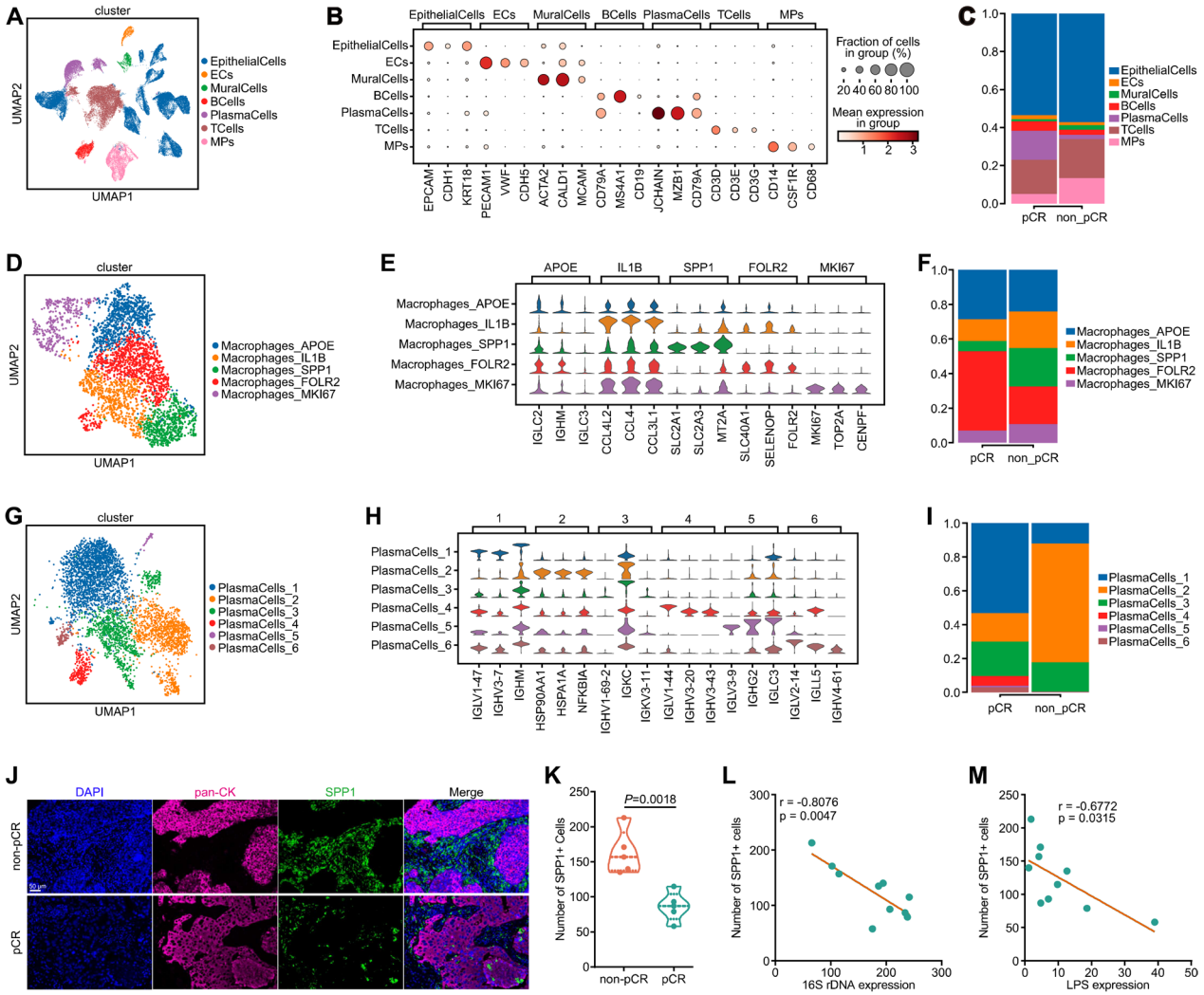

Fig. 3 Intratumoral microbiota activated anti-tumor immune. **A** UMAP plots of 7 cell types identified by scRNA-seq of 6 TNBC samples. **B** The top 3 marked genes of each cell type. **C** Statistical histograms of each cell type in pCR and non-pCR groups. **D** UMAP plots of 5 subclusters of macrophages. **E** The top 3 marked genes of each subcluster of macrophage. **F** Statistical histograms of 5 subclusters of macrophages. **G** UMAP plots of 6 subclusters of plasma cells. **H** The top 3 marked genes of each subcluster of plasma cells. **I** Statistical histograms of 6 subclusters of plasma cells. **J** mIF staining of pan-CK and SPP1 in pCR and non-pCR tumors. Scale bars, 50 μm. **K** Quantification of SPP1 + macrophages in pCR and non-pCR tumors (n = 5 in each group). **L** Correlation analysis of LPS and SPP1 + macrophages (n = 10). **M** Correlation analysis of 16S rDNA and SPP1 + macrophages (n = 10)

sensitivity of 77.3% (17/22), specificity of 78.6% (11/14), and accuracy of 77.8% (28/36). The pre-NACI model had lower accuracy (69.4%, 25/36), sensitivity (72.7%, 16/22), and specificity (64.3%, 9/14). The post-NACI model demonstrated an accuracy of 75.0% (27/36) and higher sensitivity (90.9%, 20/22) but lower specificity (50.0%, 7/14), indicating a bias toward identifying patients who achieved pCR but a limited ability to distinguish patients who did not achieve pCR. Overall, the fusion model integrated pre-NACI and post-NACI data and achieved balanced sensitivity and specificity, improving its clinical applicability for predicting tumor response to NACI. Representative patients with distinct treatment outcomes highlighted the correlation between MRI signs and histopathological findings (Fig. 6). Patients 1 and 2 (non-pCR group) exhibited heterogeneous and irregular tumor enhancement on MRI, with sparse bacterial presence and limited microbial density. In contrast, Patients 3 and 4 (pCR group) displayed reduced tumor enhancement after NACI, with significantly greater microbial density. These findings indicated the predictive value of combining imaging and intratumoral microbiome.

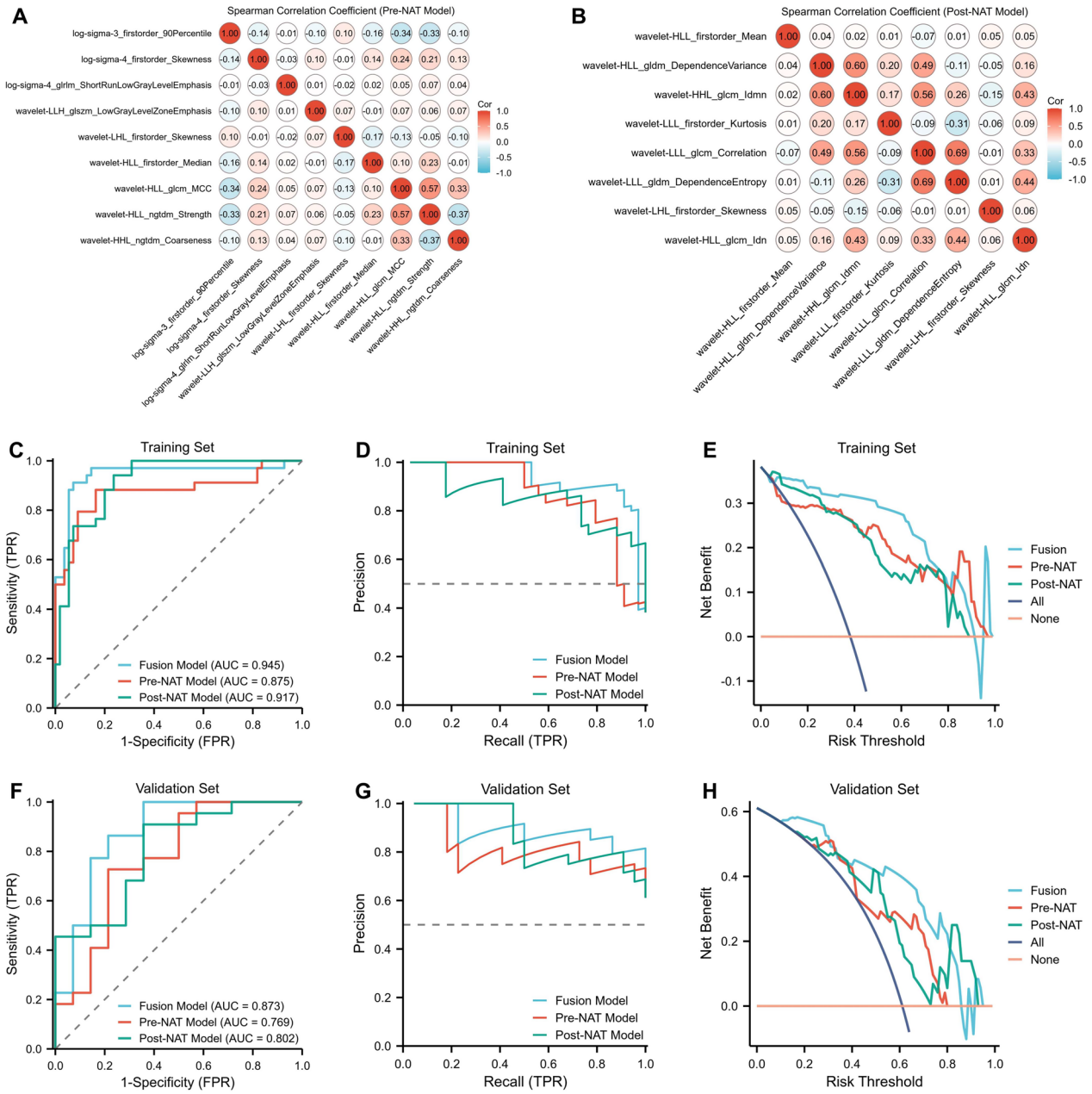

Fig. 4 Performance of pre-NACI, post-NACI, and fusion models in training and validation sets. **A**, **B** Spearman correlation heatmaps of radiomics features for the pre-NACI and post-NACI models reveal no strong correlations among features, indicating that these features are complementary. **C**, **D** Receiver Operating Characteristic and Precision-Recall Curves for the training set show that the fusion model achieves the highest AUC, outperforming the pre-NACI and post-NACI models. **E** Decision curve analysis for the training set highlights the fusion model's superior net benefit across a wide range of risk thresholds. **F**, **G** Receiver Operating Characteristic and Precision-Recall Curves for the validation set demonstrate superior performance of the fusion model compared to the pre-NACI and post-NACI models. **H** Decision curve analysis for the validation set confirms the fusion model's consistent net benefit, showcasing its clinical utility in predicting tumor response to treatment

Discussion

Although neoadjuvant chemotherapy combined with immunotherapy has been proven to be the preferable strategy for treating early-stage TNBC, only a small proportion of patients benefit from the addition of immunotherapy [5–7]. Unfortunately, powerful and specific biomarkers for predicting the efficacy of immunotherapy are still lacking. To the best of our knowledge, our current work is the first to incorporate intratumoral microbiota and radiomics to generate a specific

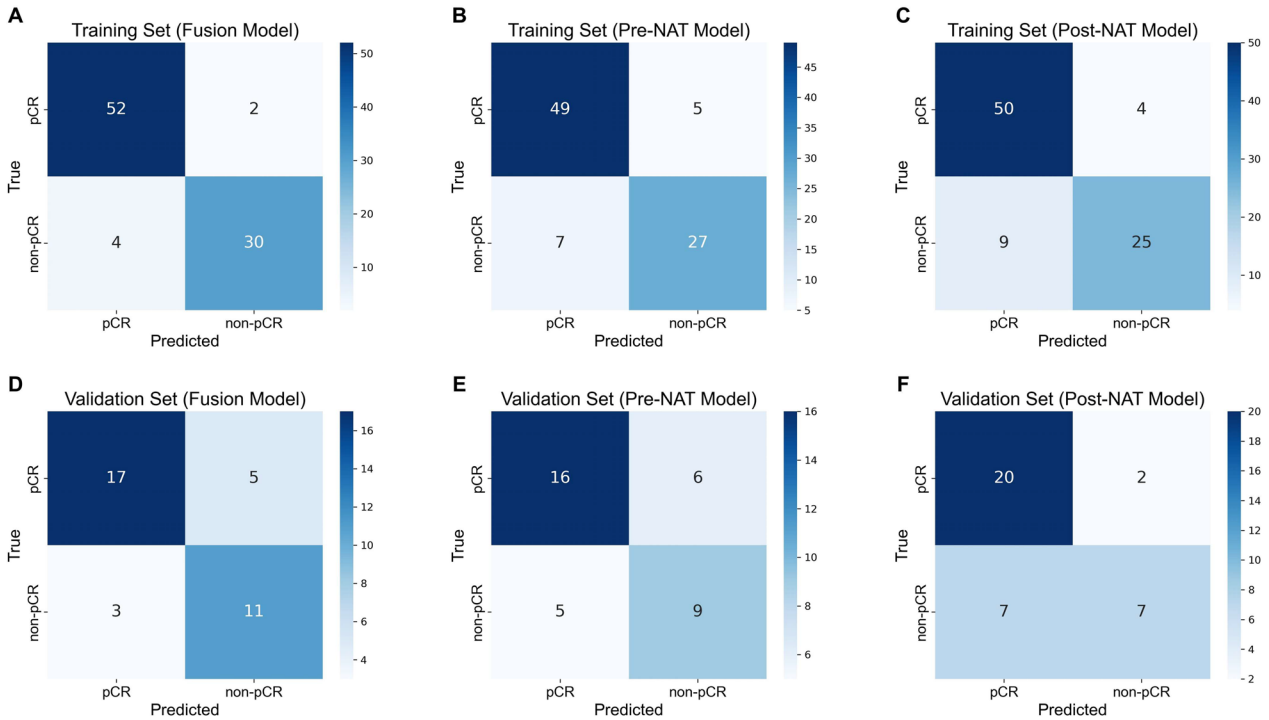

Fig. 5 Confusion matrices for predicting pCR and non-pCR cases using fusion, pre-NACI, and post-NACI models in the training and validation sets. **A**–**C** Confusion matrices for the training set using the fusion model, pre-NACI model, and post-NACI model. The fusion model demonstrates the highest accuracy, outperforming the single-timepoint models. **D**–**F** Confusion matrices for the validation set using the fusion model, pre-NACI model, and post-NACI model. The fusion model maintains strong predictive performance with a balance of true positives and true negatives, showing the robustness compared to the pre-NACI and post-NACI models

noninvasive tool for the efficacy prediction of NACI in patients with early-stage TNBC. As expected, our intratumoral microbiota-aided radiomics model significantly outperformed the models generated from pre-NACI or post-NACI MRI features, indicating a crucial role of intratumoral microbiota in individualized treatment strategy delivery.

With the development of next-generation sequencing technology, numerous tumor tissues that were previously considered sterile have also been shown to present with a large amount of intratumoral microbiota [35]. Moreover, intratumoral microbiota is usually specific to the type of tumor, indicating a pivotal association between cancer and intratumoral microbiota [19, 36]. Consequently, intratumoral microbiota has been widely applied as a powerful biomarker for cancer screening, treatment efficacy monitoring and prognosis prediction [9]. Given the observed association between antibiotic exposure and reduced clinical benefit of immunotherapy [37, 38], exploring the potential correlation between intratumoral microbiota and immunotherapy is reasonable. The role of tumor-resident microbes in modulating the TME has been widely studied [14, 39, 40]. By performing scRNA-seq analysis on tumors with different responses to NACI, we elucidated the landscape of TME in TNBC tumors and showed that intratumoral microbiota load was negatively associated with the number of tumor-associated $SPP1^{+}$ macrophages. These results suggest that intratumoral microbiota may serve as an activation modulator of tumor TME. Intriguingly, intratumoral microbiota metabolite trimethylamine N-oxide (TMAO) was reported to promote antitumor immunity in TNBC [15], suggesting that intratumoral microbiota modulates the TME of TNBC and the efficacy of NACI via their metabolites. However, the potential mechanisms need further exploration.

Recent studies have explored various imaging modalities for predicting pCR in patients with breast cancer. Huang et al. utilized longitudinal MRI for predicting pCR and B cell infiltration [41]. Urso et al. employed 18F-FDG PET/CT radiomics to predict the responses of tumors to neoadjuvant chemotherapy [42]. Additionally, Wan et al. demonstrated the potential of multimodal ultrasound radiomics for early pCR prediction [43]. These approaches highlight the increasing importance of imaging and radiomics in personalized breast cancer treatment. Radiomics features derived from MR scans before and after NACI provided complementary information on

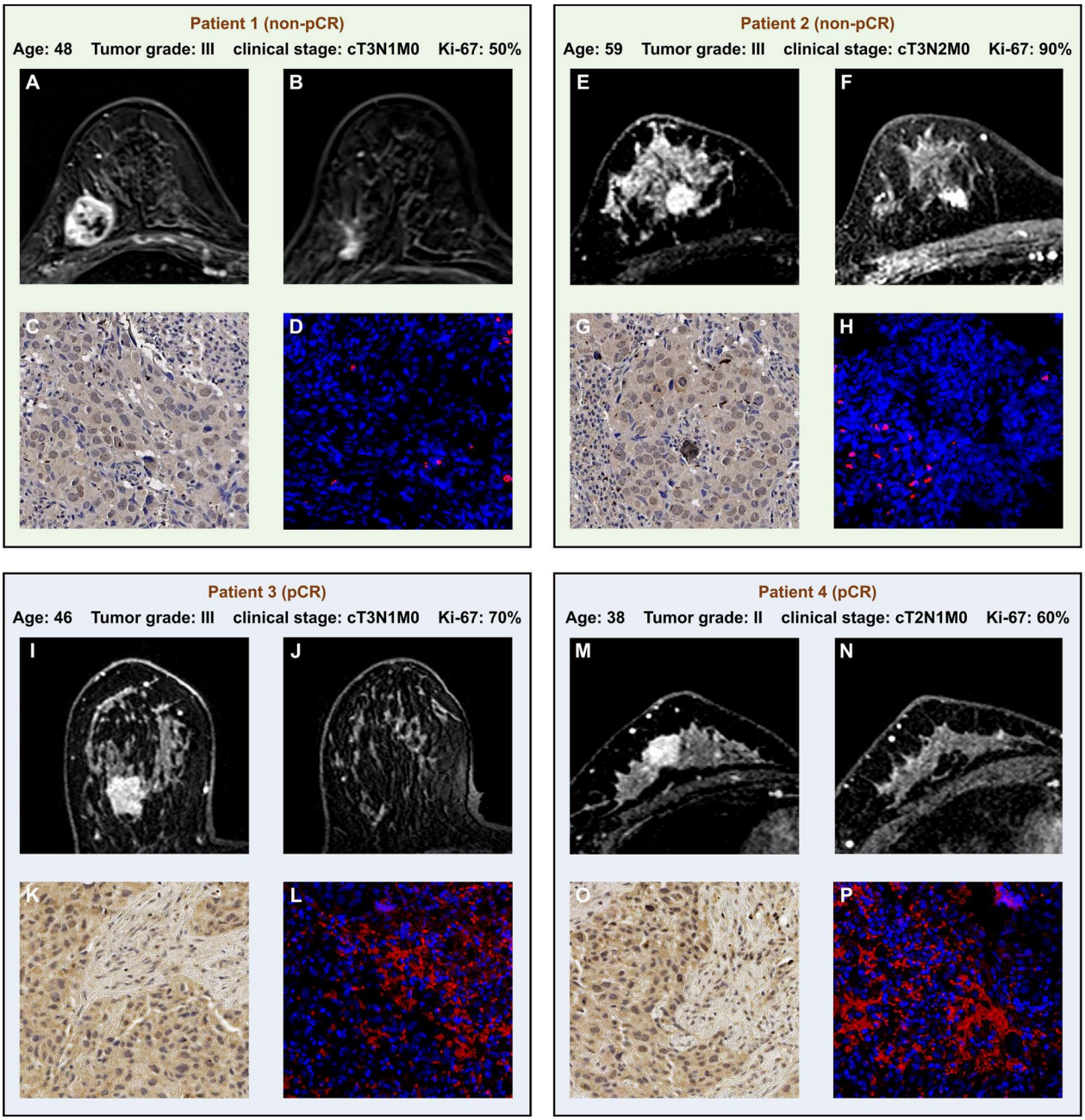

Fig. 6 Representative MRIs and histological results of breast cancer patients with pCR and non-pCR outcomes. Patient 1 (**A**–**D**) and Patient 2 (**E**–**H**): non-pCR cases show pre-NACI and post-NACI MRI images, immunohistochemistry, and immunofluorescence analysis with intratumoral microbiome counts marked in red. The two representative non-pCR patients exhibit reduced intratumoral microbiome counts. Patient 3 (**I–L**) and Patient 4 (**M**–**P**): pCR cases demonstrate pre-NACI and post-NACI MRI images, immunohistochemistry, and immunofluorescence analysis with intratumoral microbiome counts marked in red. The two representative pCR patients show increased intratumoral microbiome counts, characterized by denser cell

the tumor response to treatment [27, 44, 45]. Pre-NACI features primarily reflected baseline tumor biology, such as vascularity and cellularity, whereas post-NACI features captured dynamic changes induced by therapy, including tumor shrinkage and tissue remodeling [23, 46]. The integration of these features enabled a more accurate prediction of pCR, thus addressing the inherent limitations of single-time-point models. We subsequently developed a fusion model that integrated data from both pre- and post-NACI MRI, achieving superior

predictive performance compared with single-time-point models. Our study used elastic net regression to retain radiomics features associated with intratumoral microbiome, optimizing the interpretability and performance of the model. The fusion model captured treatment-induced morphological and functional changes, while the microbiome data added a biological dimension to the prediction. Specifically, this model outperformed both pre-NACI and post-NACI models in the training and validation sets, with the highest AUC values of 0.945 and 0.873, respectively. These findings indicated that integration of imaging biomarkers and microbiome data improved the precision of tumor response predictions, providing a noninvasive tool to guide personalized NACI.

From a clinical perspective, the fusion model demonstrated consistent performance, with a sensitivity of 77.3% and a specificity of 78.6% in the validation set. Notably, the decision curve analysis confirmed its clinical utility, demonstrating a greater net benefit in decision-making outcomes across varying risk thresholds than single-time-point models. These findings suggest that longitudinal imaging data capture dynamic changes in tumor morphology and progression, which are critical for precisely predicting tumor response. Furthermore, the balanced sensitivity and specificity of the model established it as a robust tool for distinguishing patients who achieve pCR from those who do not, fulfilling a critical clinical need for early assessment. Comparatively, single-time-point models demonstrated limitations, including the pre-NACI model's lower specificity (64.3%) and the post-NACI model's reduced accuracy (69.4%). By providing accurate predictions of NACI outcomes, the fusion model could support patient stratification, facilitate individualized treatment planning, and potentially spare non-responders from unnecessary toxic effects of chemotherapy. Most importantly, this model is constructed on the basis of MRI features, and patients with pre-treatment MRI data are eligible to be evaluated by this model, making it very easy to integrate into clinical workflows.

Limitations of our study should be acknowledged. First, potential bias in data collection may exist because of the retrospective nature and small sample sizes, especially the exclusion of patients with incomplete MRI data and unrecorded antibiotic use. For future prospective validation, patients with different intratumoral microbiota loads defined by the radiomics model should be randomly assigned to receive NACI or neoadjuvant chemotherapy alone. The exploration of different tumor types beyond TNBC and the integration of other omics data to increase the model's accuracy are necessary. Second, the sample sizes of scRNA-seq cohort (n = 6) and validation cohort (n = 36) were underpowered to capture intratumoral microbiota diversity or rare immune subsets, necessitating larger cohorts to validate the $SPP1^{+}$ macrophage results. Our study population consisted of patients from only two centers in China, and we acknowledge that the sample may not fully represent diverse ethnicities and geographic regions. Moreover, pCR, rather than long-term survival outcomes such as overall survival and disease-free survival, was chosen as the main endpoint for evaluating intratumoral microbiota and constructing a radiomics model owing to the relatively short follow-up duration. Finally, the mechanisms by which intratumoral microbiota modulates the TME have not been elucidated.

Conclusions

In summary, we explored and validated intratumoral microbiota as a powerful predictor of the response of patients with early-stage TNBC to NACI. Moreover, we developed an intratumoral microbiota-aided fusion radiomics model that showed strong power in predicting the response of patients to NACI. Our findings provide a noninvasive and powerful tool for the development of individualized NACI strategies to treat patients with early-stage TNBC.

Abbreviations

NACI	Neoadjuvant chemoimmunotherapy
TNBC	Triple-negative breast cancer
16S-seq	16S rDNA sequencing
scRNA-seq	Single-cell transcriptome sequencing
TME	Tumor microenvironment
MRIs	Magnetic resonance images
pCR	Pathological complete response
AUC	Area under the curve
DCE	Dynamic contrast-enhanced
ROC	Receiver operating characteristic
PR	Precision-recall
DCA	Decision curve analysis
RT-qPCR	Real-time quantitative polymerase chain reaction
CR	Complete response
mIF	Multiplex immunofluorescence
2D	Two-dimensional
3D	Three-dimensional

Supplementary Information

The online version contains supplementary material available at https://doi.org/10.1186/s12967-025-06369-7.

Additional file 1.

Acknowledgements

Not applicable.

Author contributions

Concept and design: K.W. and H.P. Analysis and interpretation of data: Y.L.C., Y.H.H., W.L., T.Z., M.Y.C. and L.L.Z. Drafting of article: Y.L.C., Y.H.H. and W.L. All authors read and approved the final manuscript.

Funding

This study is supported by grants from National Natural Science Foundation of China (82171898, 82372726), Deng Feng project of high-level hospital

construction (DFJHBF202109), Macao Science and Technology Development Fund (0021070118131610 6/AKP) and Beijing Life Oasis Public Service Center (cphcf-2022–058).

Availability of data and materials
The datasets produced during our study are available from the corresponding authors for scientific research.

Declarations

Ethics approval and consent to participate
Written informed consent for the use of patient specimens was obtained from each participant. The study protocols were approved by the Research Ethics Committee of Guangdong Provincial People's Hospital and the First People's Hospital of Foshan.

Consent for publication
Not applicable.

Competing interests
The authors declared no competing interests.

Author details
[1]School of Medicine, South China University of Technology, Guangzhou 510006, China. [2]Department of Breast Cancer, Guangdong Provincial People's Hospital (Guangdong Academy of Medical Sciences), Southern Medical University, 106 Zhongshan Er Road, Yuexiu District, Guangzhou 510080, People's Republic of China. [3]Department of Breast Cancer, The First People's Hospital of Foshan, 81 Lingnan Road North, Chancheng District, Foshan 528000, People's Republic of China. [4]The Second School of Clinical Medicine, Southern Medical University, Guangzhou 510515, People's Republic of China.

Received: 19 December 2024 Accepted: 8 March 2025
Published online: 20 March 2025

References

1. Leon-Ferre RA, Goetz MP. Advances in systemic therapies for triple negative breast cancer. BMJ. 2023;381: e071674.
2. Waks AG, Winer EP. Breast cancer treatment: a review. JAMA. 2019;321(3):288–300.
3. Bianchini G, De Angelis C, Licata L, Gianni L. Treatment landscape of triple-negative breast cancer—expanded options, evolving needs. Nat Rev Clin Oncol. 2022;19(2):91–113.
4. Denkert C, Liedtke C, Tutt A, von Minckwitz G. Molecular alterations in triple-negative breast cancer-the road to new treatment strategies. Lancet. 2017;389(10087):2430–42.
5. Schmid P, Cortes J, Dent R, Pusztai L, McArthur H, Kummel S, et al. Event-free survival with pembrolizumab in early triple-negative breast cancer. N Engl J Med. 2022;386(6):556–67.
6. Schmid P, Cortes J, Pusztai L, McArthur H, Kummel S, Bergh J, et al. Pembrolizumab for early triple-negative breast cancer. N Engl J Med. 2020;382(9):810–21.
7. Schmid P, Cortes J, Dent R, McArthur H, Pusztai L, Kummel S, et al. Overall survival with pembrolizumab in early-stage triple-negative breast cancer. N Engl J Med. 2024;391(21):1981–91.
8. de Martel C, Georges D, Bray F, Ferlay J, Clifford GM. Global burden of cancer attributable to infections in 2018: a worldwide incidence analysis. Lancet Glob Health. 2020;8(2):e180–90.
9. Dai JH, Tan XR, Qiao H, Liu N. Emerging clinical relevance of microbiome in cancer: promising biomarkers and therapeutic targets. Protein Cell. 2024;15(4):239–60.
10. Fu A, Yao B, Dong T, Chen Y, Yao J, Liu Y, et al. Tumor-resident intracellular microbiota promotes metastatic colonization in breast cancer. Cell. 2022;185(8):1356-72.e1326.
11. Fu K, Cheung AHK, Wong CC, Liu W, Zhou Y, Wang F, et al. *Streptococcus anginosus* promotes gastric inflammation, atrophy, and tumorigenesis in mice. Cell. 2024;187(4):882-96.e817.
12. Jia D, Wang Q, Qi Y, Jiang Y, He J, Lin Y, et al. Microbial metabolite enhances immunotherapy efficacy by modulating T cell stemness in pan-cancer. Cell. 2024;187(7):1651-65.e21.
13. Park EM, Chelvanambi M, Bhutiani N, Kroemer G, Zitvogel L, Wargo JA. Targeting the gut and tumor microbiota in cancer. Nat Med. 2022;28(4):690–703.
14. Qiao H, Tan XR, Li H, Li JY, Chen XZ, Li YQ, et al. Association of intratumoral microbiota with prognosis in patients with nasopharyngeal carcinoma from 2 hospitals in China. JAMA Oncol. 2022;8(9):1301–9.
15. Wang H, Rong X, Zhao G, Zhou Y, Xiao Y, Ma D, et al. The microbial metabolite trimethylamine N-oxide promotes antitumor immunity in triple-negative breast cancer. Cell Metab. 2022;34(4):581-94.e588.
16. Garrett WS. Cancer and the microbiota. Science. 2015;348(6230):80–6.
17. Yang L, Li A, Wang Y, Zhang Y. Intratumoral microbiota: roles in cancer initiation, development and therapeutic efficacy. Signal Transduct Target Ther. 2023;8(1):35.
18. Tanoue T, Morita S, Plichta DR, Skelly AN, Suda W, Sugiura Y, et al. A defined commensal consortium elicits CD8 T cells and anti-cancer immunity. Nature. 2019;565(7741):600–5.
19. Nejman D, Livyatan I, Fuks G, Gavert N, Zwang Y, Geller LT, et al. The human tumor microbiome is composed of tumor type-specific intracellular bacteria. Science. 2020;368(6494):973–80.
20. Bender MJ, McPherson AC, Phelps CM, Pandey SP, Laughlin CR, Shapira JH, et al. Dietary tryptophan metabolite released by intratumoral *Lactobacillus reuteri* facilitates immune checkpoint inhibitor treatment. Cell. 2023;186(9):1846–62.
21. Sun Z, Zhang T, Ahmad MU, Zhou Z, Qiu L, Zhou K, et al. Comprehensive assessment of immune context and immunotherapy response via noninvasive imaging in gastric cancer. J Clin Invest. 2024;134(6): e175834.
22. Qi YJ, Su GH, You C, Zhang X, Xiao Y, Jiang YZ, et al. Radiomics in breast cancer: current advances and future directions. Cell Rep Med. 2024;5(9):101719.
23. Feng Z, Li H, Liu Q, Duan J, Zhou W, Yu X, et al. CT radiomics to predict macrotrabecular-massive subtype and immune status in hepatocellular carcinoma. Radiology. 2023;307(1): e221291.
24. Braman NM, Etesami M, Prasanna P, Dubchuk C, Gilmore H, Tiwari P, et al. Intratumoral and peritumoral radiomics for the pretreatment prediction of pathological complete response to neoadjuvant chemotherapy based on breast DCE-MRI. Breast Cancer Res. 2017;19(1):57.
25. Liu Z, Li Z, Qu J, Zhang R, Zhou X, Li L, et al. Radiomics of multiparametric MRI for pretreatment prediction of pathologic complete response to neoadjuvant chemotherapy in breast cancer: a multicenter study. Clin Cancer Res. 2019;25(12):3538–47.
26. Li J, Cao Y, Liu Y, Yu L, Zhang Z, Wang X, et al. Multiomics profiling reveals the benefits of gamma-delta (gammadelta) T lymphocytes for improving the tumor microenvironment, immunotherapy efficacy and prognosis in cervical cancer. J Immunother Cancer. 2024;12(1): e008355.
27. Liu L, Xu L, Wu D, Zhu Y, Li X, Xu C, et al. Impact of tumour stroma-immune interactions on survival prognosis and response to neoadjuvant chemotherapy in bladder cancer. EBioMedicine. 2024;104:105152.
28. Ramtohul T, Lepagney V, Bonneau C, Jin M, Menet E, Sauge J, et al. Use of pretreatment perfusion MRI-based intratumoral heterogeneity to predict pathologic response of triple-negative breast cancer to neoadjuvant chemoimmunotherapy. Radiology. 2024;312(3): e240575.
29. Liu Y, Xun Z, Ma K, Liang S, Li X, Zhou S, et al. Identification of a tumour immune barrier in the HCC microenvironment that determines the efficacy of immunotherapy. J Hepatol. 2023;78(4):770–82.
30. Matusiak M, Hickey JW, van IJzendoorn DGP, Lu G, Kidzinski L, Zhu S, et al. Spatially segregated macrophage populations predict distinct outcomes in colon cancer. Cancer Discov. 2024;14(8):1418–39.
31. Wang Y, Wang Q, Tao S, Li H, Zhang X, Xia Y, et al. Identification of SPP1(+) macrophages in promoting cancer stemness via vitronectin and CCL15 signals crosstalk in liver cancer. Cancer Lett. 2024;604:217199.
32. Yang Z, Tian H, Chen X, Li B, Bai G, Cai Q, et al. Single-cell sequencing reveals immune features of treatment response to neoadjuvant immunochemotherapy in esophageal squamous cell carcinoma. Nat Commun. 2024;15(1):9097.

33. Ozato Y, Kojima Y, Kobayashi Y, Hisamatsu Y, Toshima T, Yonemura Y, et al. Spatial and single-cell transcriptomics decipher the cellular environment containing HLA-G+ cancer cells and SPP1+ macrophages in colorectal cancer. Cell Rep. 2023;42(1):111929.
34. Sathe A, Mason K, Grimes SM, Zhou Z, Lau BT, Bai X, et al. Colorectal cancer metastases in the liver establish immunosuppressive spatial networking between tumor-associated SPP1+ macrophages and fibroblasts. Clin Cancer Res. 2023;29(1):244–60.
35. Erb-Downward JR, Falkowski NR, D'Souza JC, McCloskey LM, McDonald RA, Brown CA, et al. Critical relevance of stochastic effects on low-bacterial-biomass 16S rRNA gene analysis. MBio. 2020;11(3):e00258-e320.
36. Narunsky-Haziza L, Sepich-Poore GD, Livyatan I, Asraf O, Martino C, Nejman D, et al. Pan-cancer analyses reveal cancer-type-specific fungal ecologies and bacteriome interactions. Cell. 2022;185(20):3789-806. e3717.
37. Derosa L, Hellmann MD, Spaziano M, Halpenny D, Fidelle M, Rizvi H, et al. Negative association of antibiotics on clinical activity of immune checkpoint inhibitors in patients with advanced renal cell and non-small-cell lung cancer. Ann Oncol. 2018;29(6):1437–44.
38. Routy B, Le Chatelier E, Derosa L, Duong CPM, Alou MT, Daillere R, et al. Gut microbiome influences efficacy of PD-1-based immunotherapy against epithelial tumors. Science. 2018;359(6371):91–7.
39. Galeano Niño JL, Wu H, LaCourse KD, Kempchinsky AG, Baryiames A, Barber B, et al. Effect of the intratumoral microbiota on spatial and cellular heterogeneity in cancer. Nature. 2022;611(7937):810–7.
40. Cao Y, Xia H, Tan X, Shi C, Ma Y, Meng D, et al. Intratumoural microbiota: a new frontier in cancer development and therapy. Signal Transduct Target Ther. 2024;9(1):15.
41. Huang YH, Shi ZY, Zhu T, Zhou TH, Li Y, Li W, et al. Longitudinal MRI-driven multi-modality approach for predicting pathological complete response and b cell infiltration in breast cancer. Adv Sci. 2025. https://doi.org/10.1002/advs.202413702.
42. Urso LA-O, Manco LA-O, Cittanti CA-OX, Adamantiadis S, Szilagyi KA-O, Scribano GA-O, et al. (18)F-FDG PET/CT radiomic analysis and artificial intelligence to predict pathological complete response after neoadjuvant chemotherapy in breast cancer patients. Radiol Med. 2025. https://doi.org/10.1007/s11547-025-01958-4.
43. Wan CF, Jiang ZY, Wang YQ, Wang L, Fang H, Jin Y, et al. Radiomics of multimodal ultrasound for early prediction of pathologic complete response to neoadjuvant chemotherapy in breast cancer. Acad Radiol. 2024. https://doi.org/10.1016/j.acra.2024.11.012.
44. Chen D, Zhang R, Huang X, Ji C, Xia W, Qi Y, et al. MRI-derived radiomics assessing tumor-infiltrating macrophages enable prediction of immune-phenotype, immunotherapy response and survival in glioma. Biomark Res. 2024;12(1):14.
45. Crispin-Ortuzar M, Woitek R, Reinius MAV, Moore E, Beer L, Bura V, et al. Integrated radiogenomics models predict response to neoadjuvant chemotherapy in high grade serous ovarian cancer. Nat Commun. 2023;14(1):6756.
46. Jiang L, You C, Xiao Y, Wang H, Su GH, Xia BQ, et al. Radiogenomic analysis reveals tumor heterogeneity of triple-negative breast cancer. Cell Rep Med. 2022;3(7):100694.

Publisher's Note